Physics in Medicine & Biology

PAPER

Optimal multichannel transmission for improved cr-MREPT

To cite this article: Gokhan Ariturk and Yusuf Ziya Ider 2018 *Phys. Med. Biol.* **63** 045001

IOP Publishing Phys. Med. Biol. 63 (2018) 045001 (14pp) https://doi.org/10.1088/1361-6560/aaa732

Physics in Medicine & Biology

IPEM Institute of Physics and Engineering in Medicine

PAPER

Optimal multichannel transmission for improved cr-MREPT

Gokhan Ariturk[1] and Yusuf Ziya Ider[1,2]

[1] Department of Electrical and Electronics Engineering, Bilkent University, Ankara, Turkey
[2] Author to whom any correspondence should be addressed.

E-mail: ider@ee.bilkent.edu.tr

RECEIVED
2 October 2017

REVISED
22 December 2017

ACCEPTED FOR PUBLICATION
12 January 2018

PUBLISHED
8 February 2018

Keywords: electrical properties, electrical properties tomography, multichannel RF transmission, multichannel transceiver array, B1 shimming, EPT

Abstract

Magnetic resonance electrical properties tomography (MR-EPT), aiming at reconstructing the EP's at radio frequencies, uses the H^+ field (both magnitude and phase) distribution within the object. One of the MR-EPT algorithms, cr-MREPT, accurately reconstructs the internal tissue boundaries, however, it faces an artifact which occurs at the regions where the convective field, $\left[\frac{\partial H^+}{\partial x} - \mathrm{i}\frac{\partial H^+}{\partial y}, \mathrm{i}(\frac{\partial H^+}{\partial x} - \mathrm{i}\frac{\partial H^+}{\partial y})\right]^T$, has a low magnitude (at the noise level). This study aims to develop an artifact-free conductivity reconstruction by modifying the H^+ field inside the region of interest (ROI), using multiple RF transmission techniques in MRI. An eight channel multi-transmit transverse electromagnetic array is used in two different drive configurations. The first drive is the standard volume excitation configuration where all ports are driven with the same magnitude and with 45° phase increment between adjacent channels. In the second drive, the drive voltage magnitude and phases for each of the eight drive ports are modified to generate a desired H^+ distribution such that the low convective field region moves to another non-overlapping position. Finally, data from both drive experiments are simultaneously used to reconstruct EP's. Computer simulations using cylindrical phantoms and a brain model are conducted and it is shown that the low convective field artifact can be eliminated. It is further shown that it is not necessary to re-calculate the port drive RF voltage magnitude and phases for each patient. The implementation issues of this method are briefly discussed.

1. Introduction

Electrical tissue properties (EP's), namely, electrical conductivity (σ) and permittivity (ϵ), provide important clinical information about cancerous tissues as well as being useful in distinguishing between ischemic and hemorrhagic stroke (Surowiec *et al* 1988, Holder 1993, Joines *et al* 1994). They are also important in finding the specific absorption rate (SAR) in tissues during magnetic resonance imaging (MRI) scans and also in inverse problems of electrophysiology (Liu *et al* 2006, He *et al* 2011).

In general, EP's are frequency dependent (Gabriel *et al* 1996). Previous techniques, aiming at imaging tissue properties such as electrical impedance tomography (EIT) (Romsauerova *et al* 2006), magnetic resonance electrical impedance tomography (MR-EIT) (Birgul and Ider 1995, Ider and Birgul 1998) and magnetic induction tomography (MIT) (Griffiths 2001) reconstruct the tissue properties at frequencies mostly lower than 100 kHz. A more recent technique, magnetic resonance—electrical properties tomography (MR-EPT) makes use of MRI technology and aims at reconstructing tissue properties at radio frequencies.

MR-EPT studies provide either pointwise (local) or global EP reconstructions (Liu *et al* 2017). In pointwise EP reconstructions (Nachman *et al* 2007, Voigt *et al* 2011, Van Lier *et al* 2012), including the Helmholtz's equation based standard (conventional) MREPT (Voigt *et al* 2011), the EP reconstruction on a certain pixel is only affected by the H^+ data on itself and by the H^+ data on nearby pixels. This is due to the application of Laplacian operator and some filter kernels during EP reconstruction (Liu *et al* 2017). On the other hand, global studies such as convection-reaction equation based MREPT (cr-MREPT) (Hafalir *et al* 2014, Gurler and Ider 2016), gradient-based MR-EPT (g-EPT) (Liu *et al* 2015) and contrast source inversion EPT (CSI- EPT) (Balidemaj *et al* 2015) reconstruct the EP's by solving the EPT equations over the entire region of interest. In these studies, each pixel/

voxel of the reconstructed EP's are affected (constrained) by the inter-voxel relations and hence, they tend to be less prone to noise contamination.

Another criterion used in comparing MR-EPT algorithms is whether they make the assumption of homogeneous EP distribution in the region of interest (ROI). Algorithms described in Voigt *et al* (2011) and Van Lier *et al* (2012) assume that the EP's are slowly varying over the ROI, and they give inaccurate reconstructions at tissue boundaries where EP's may drastically vary (Liu *et al* 2017). On the other hand, methods described in Hafalir *et al* (2014), Balidemaj *et al* (2015), Liu *et al* (2015) and Gurler and Ider (2016), including cr-MREPT, do not make the assumption of homogeneous EP distributions and therefore the EP's at the tissue boundaries are better reconstructed.

Regarding the global studies, the CSI-EPT method is based on the constrained minimization of a cost function which is norm of the difference between measured and calculated B_1^+ distributions. The calculated B_1^+ is found by solving a forward model of the MRI coil system and the object, which relates B_1^+ to the electrical properties of the object. Although this method is robust against noise, it is computationally demanding since it requires the handling of the problem in a 3D setting as well as an accurate model of the MRI system. A similar method, global maxwell tomography (GMT), which is based on integral equations, solely makes use of the B_1^+ field magnitude and it has only been tested with numerical simulation phantoms (Serralles *et al* 2017). The g-EPT method, calculating the derivatives of the absolute and relative transmit B_1^+ phases works very well for ultra-high fields ($\geqslant$7 T), however, the technique requires too many experiments with different transmit-receive configurations from various channels of a multitransmit array for reconstructing the relative and absolute phases of the B_1^+ field. Another variant of the global algorithms described in Borsic *et al* (2016) and Ropella and Noll (2017) make local homogeneity assumption in their forward problem formulations (e.g. they use the formulation $\nabla^2\phi^+ = \omega\mu_0\sigma$ to calculate ϕ^+ (phase of B_1^+) from a given distribution, where $\omega = 2\pi f_0$ and f_0 is the Larmor frequency), but solve the inverse problem in the global sense by fitting measured data to the calculated data. Nevertheless, they need to make heavy use of regularization techniques to constrain their solutions for not having excess variations near the boundaries. Finally, the cr-MREPT method can reconstruct EP's with a single experiment, however, it uses the transceive phase approximation (TPA) (Katscher *et al* 2009) for acquiring the phase of the B_1^+ field.

For the g-EPT method, in regions where $\frac{\partial H^+}{\partial x} - \mathrm{i}\frac{\partial H^+}{\partial y}$ has low magnitude, a global bias in the EP reconstructions is observed (Liu *et al* 2017) ($H^+ = (H_x + \mathrm{i}H_y)/2$) is the MR-wise important rotating RF magnetic field during transmission). Likewise for the cr-MREPT method, a spot-like artifact arises in such regions (Hafalir *et al* 2014, Li *et al* 2017). In cr-MREPT studies, $\left[\frac{\partial H^+}{\partial x} - \mathrm{i}\frac{\partial H^+}{\partial y}, \mathrm{i}(\frac{\partial H^+}{\partial x} - \mathrm{i}\frac{\partial H^+}{\partial y})\right]^T$ is referred to as the 'convective field' and the spot-like artifact is called the low convective field (LCF) artifact. In particular, EP reconstructions attain significantly incorrect values (generally abruptly occurring peaks or dips) at the regions of LCF artifact (Hafalir *et al* 2014). More importantly, the EP reconstruction performance of the cr-MREPT algorithm is significantly reduced where a tissue boundary coincides with an LCF region and this means that the main advantage of the cr-MREPT algorithm is severely distorted.

In order to alleviate the obstructions, brought forth by the low convective fields, methods that are altering the B_1^+ distribution are proposed. One of these methods developed in Yildiz *et al* (2017) uses materials with high dielectric constants for padding around the object and aims at altering the B_1^+ magnitude distribution within the object. With wisely located dielectric pads, spatial shift of the LCF regions is accomplished and as a result, the locations of the LCF artifacts are also shifted. Finally, two set of equations utilizing the B_1^+ distributions with and without padding are simultaneously solved to obtain an artifact-free reconstruction (Yildiz *et al* 2017).

Another study, working on reducing the LCF-related artifacts, was presented in Gurler *et al* (2015) and Gurler (2016) and solves the B_1^- based cr-MREPT equation ($B_1^- = (H_x - \mathrm{i}H_y)^*/2$), merging the data from different channels of a multi-receive coil. When a four channel phased array type receive head coil is used, the LCF regions for all channels overlap in the middle of the object. Therefore, it is not possible to eliminate central LCF artifacts, although the method is successful in non-central ROIs.

In the proposed study, we developed an artifact-free conductivity reconstruction algorithm which uses two different B_1^+ distributions being obtained by two different simulated multichannel RF drive configurations. These B_1^+ distributions are obtained using an eight-channel transverse electromagnetic (TEM) array being designed for 3T MRI systems. In the first drive (normal drive), the conventional birdcage-like volume coil excitation is applied where B_1^+ magnitude exhibits the usual 'central brightening' behavior and the LCF region occurs roughly at the center of the object. In the second drive (modified drive), the B_1^+ magnitude at the center of the object is varied by applying optimized input RF sinusoids to the input ports of the TEM array. This B_1^+ magnitude variation shifts the LCF region away from the center such that the LCF regions in normal and modified drive experiments do not overlap. Finally, B_1^+ distributions from these two drive cases are simultaneously used to converge on a single artifact-free EP reconstruction as in Hafalir *et al* (2014).

Commencing with the theory behind the cr-MREPT method, this paper elucidates the reason of the LCF artifact and gives the logic behind the applied procedure. In continuation, simulation methods are explained

and reconstruction results of three different simulation phantoms (including the head model) are given. Finally, practical implementation issues related to this method are discussed.

2. Theory

2.1. cr-MREPT theory

The cr-MREPT method (Hafalir *et al* 2014) is based on the solution of the following convection-reaction partial differential equation for the unknown 'u':

$$\boldsymbol{\beta} \cdot \nabla u + \nabla^2 H^+ u - \mathrm{i}\omega\mu_0 H^+ = 0 \tag{1}$$

where $u = 1/\gamma, \gamma = \sigma + \mathrm{i}\omega\epsilon$,

$$\boldsymbol{\beta} = \begin{bmatrix}\beta_x\\ \beta_y\\ \beta_z\end{bmatrix} = \begin{bmatrix}\frac{\partial H^+}{\partial x} - \mathrm{i}\frac{\partial H^+}{\partial y} + \frac{1}{2}\frac{\partial H_z}{\partial z}\\ \mathrm{i}\frac{\partial H^+}{\partial x} + \frac{\partial H^+}{\partial y} + \frac{\mathrm{i}}{2}\frac{\partial H_z}{\partial z}\\ \frac{\partial H^+}{\partial z} - \frac{1}{2}\frac{\partial H_z}{\partial x} - \frac{\mathrm{i}}{2}\frac{\partial H_z}{\partial y}\end{bmatrix}, \nabla u = \begin{bmatrix}\partial u/\partial x\\ \partial u/\partial y\\ \partial u/\partial z\end{bmatrix}.$$

This equation, having the convection term as $\boldsymbol{\beta} \cdot \nabla u$ and the reaction term as $\nabla^2 H^+ u - \mathrm{i}\omega\mu_0 H^+$ can either be solved in three dimensions or it can be solved in two dimensions for only the slice of interest, by neglecting the derivatives of H_z, and the z-derivatives of H^+ as in Hafalir *et al* (2014). When considered in two dimensions, equation (1) reduces to equation (2), which is given by:

$$\boldsymbol{F} \cdot \bar{\nabla} u + \bar{\nabla}^2 H^+ u - \mathrm{i}\omega\mu_0 H^+ = 0 \tag{2}$$

where

$$\boldsymbol{F} = \begin{bmatrix}F_x\\ F_y\end{bmatrix} = \begin{bmatrix}\frac{\partial H^+}{\partial x} - \mathrm{i}\frac{\partial H^+}{\partial y}\\ \mathrm{i}\frac{\partial H^+}{\partial x} + \frac{\partial H^+}{\partial y}\end{bmatrix}, \bar{\nabla} u = \begin{bmatrix}\frac{\partial u}{\partial x}\\ \frac{\partial u}{\partial y}\end{bmatrix}.$$

For this case, $\boldsymbol{F} \cdot \bar{\nabla} u$ is the convection term and $\boldsymbol{F}$ is the 'convective field'. H^+ and therefore $\boldsymbol{F}$ are obtained from the simulations. It should be noted that the y-component of the vector $\boldsymbol{F}$ is the complex number i times its x-component. Therefore, in order to observe and analyze the properties of $\boldsymbol{F}$, it suffices to investigate F_x.

As explained in Hafalir *et al* (2014), equation (2) is discretized on a triangular mesh and a system of linear cr-MREPT equations is obtained with the number of equations being equal to the number of triangular elements in the mesh. In this case, the number of unknown 'u's is equal to the number of the nodes. The 'u' values at the external boundary nodes are assumed to be known. It is observed that inaccurate boundary values distort the solution for only a few layers of nodes towards the interior of the object. Conductivity and relative permittivity are extracted from the solution using $\sigma = \mathrm{Re}\{1/u\}$ and $\epsilon_r = (1/\omega\epsilon_0)(\mathrm{Im}\{1/u\})$.

It was reported in Hafalir *et al* (2014) and Li *et al* (2017) that the permittivity reconstructions of cr-MREPT tend to give overestimated results at the regions with higher conductivities compared to their surroundings and that permittivity reconstructions are much more vulnerable to noise contamination. Therefore, in contrast to the conductivity results, all of the relative permittivity reconstructions except for the ones in 'homogeneous phantom' are obtained after filtering the B_1^+ data with a 2D Gaussian filter having a kernel size of 3×3 and a standard deviation of 2.

When two sets of data are collected for the same object such as in padding studies (Hafalir *et al* 2014, Yildiz *et al* 2017) or as in this study where data for normal drive and modified drive are collected, the two systems of cr-MREPT equations obtained using the two sets of data are simultaneously solved. The results obtained from this simultaneous solution are called 'combined conductivity' and 'combined permittivity' images.

2.2. Observations regarding the LCF

As mentioned above, the LCF artifact, occurring at the regions where magnitude of the convective field $\boldsymbol{F}$ attains a value of zero (or a value comparable to noise), has a behavior characterized by abrupt and significant point-wise jumps at the EP reconstructions obtained by the cr-MREPT method.

To propose a solution based on shifting the LCF artifact, we make several observations on the relation between electric field, H^+ field, and the LCF region.

Considering the definition of F_x in equation (2) and using ($H^+ = (H_x + \mathrm{i}.H_y)/2$), one gets

$$F_x = \frac{1}{2}\left[\frac{\partial H_x}{\partial x} + \frac{\partial H_y}{\partial y} + \mathrm{i}\left(\frac{\partial H_y}{\partial x} - \frac{\partial H_x}{\partial y}\right)\right]. \tag{3}$$

Using the fact that $\nabla \cdot \boldsymbol{H} = 0$ and assuming $\frac{\partial H_z}{\partial z}$ is negligible, we obtain the simplified expression

$$F_x \approx (\mathrm{i}/2)(\partial H_y/\partial x - \partial H_x/\partial y). \tag{4}$$

Finally, using the z-component of the Ampere's law, one can show that

$$2\mathrm{i}F_x = \gamma E_z. \tag{5}$$

This equation implies that magnitude of the convective field $\boldsymbol{F}$ attains low values where γE_z, being the sum of conduction and displacement currents, is low. As the electric field, and hence the current density at a certain region drops it will no longer provide a B_1^+ contribution which would contain information for reconstructing the EP's at that region. This corollary guides us with the inference that we need to shift the region where the z-component of the electric field becomes low in order to shift the location of the LCF artifact.

Considering the conventional birdcage coil systems used in MRI RF transmission, the coil produces a B_1^+ or, equivalently a $\mu_0 H^+$ field with a maximum magnitude and minimum phase at the center, when a cylindrical and homogeneous electrical properties phantom is located inside. Furthermore, the magnitude and phase of the H^+ become more and more constant as we reach the center of the phantom. Regarding equation (4) therefore, it becomes not surprising to have an LCF artifact at the center of a homogeneous phantom due to the vanishing derivative terms. In this regard, our proposal for shifting the LCF region is to perform a B_1^+ modification with the goal of having a varying $B_1^+ = \mu_0 H^+$ magnitude at the middle region of the object. The magnitude-based B_1^+ modification will be explained in the following section.

3. Methods

3.1. B_1^+ modification for shifting the LCF region

The B_1^+ modification inside the phantom was carried out with the magnitude and phase adjustment of the RF inputs at the channel input ports of the TEM array which is described in the next section. The procedure, which has been invoked in different studies such as (Abraham and Ibrahim 2007, Van den Berg *et al* 2007) is explained as follows:

We start by calling the B_1^+ distribution inside a region of interest, which is interior to our simulation phantom, as $\boldsymbol{B1}^+(V_1, \phi_1, V_2, \phi_2, ...V_8, \phi_8) = \boldsymbol{B1}^+(\boldsymbol{\theta})$, where V_n and ϕ_n such that $n \in \{1, 2, 3, 4, 5, 6, 7, 8\}$ are the amplitudes and phases of the RF inputs, applied from the n'th port respectively. $\boldsymbol{B1}^+$ is the discretized complex B_1^+ distribution vector (organized as one column) and $\boldsymbol{\theta}$ is the RF input parameter vector such that $\boldsymbol{\theta} = [V_1, \phi_1, V_2, \phi_2, ..., V_8, \phi_8]^T$. Due to the superposition principle, we can say that the B_1^+ field, generated by the eight RF input channels simultaneously, is equal to the sum of the B_1^+ fields generated by the individual RF input channels as in equation (6).

$$\boldsymbol{B1}^+(\boldsymbol{\theta}) = \sum_{n=1}^{N_{\text{channel}}} V_n \mathrm{e}^{(\mathrm{i}\phi_n)} \boldsymbol{B1}^{n+}(1V, 0°) \tag{6}$$

where N_{channel} is the number of RF channels (ports) and $\boldsymbol{B1}^{n+}(1\text{ V}, 0°)$ is the B_1^+ distribution due to the nth individual channel, when all the channels except for the nth channel are reference impedance (50 Ω) terminated (not driven by RF signal) and the nth channel is driven with RF amplitude and phase values of 1 V and 0°, respectively. In this regard, we can define the $\boldsymbol{\theta}$ dependent cost function as:

$$C(\boldsymbol{\theta}) = \sum_{i=1}^{M} (|B1_i^+(\boldsymbol{\theta})| - |B1_i^{+,\text{goal}}|)^2 \tag{7}$$

where M is the total number of elements in the $\boldsymbol{B1}^+(\boldsymbol{\theta})$ vector, $B1_i^+(\boldsymbol{\theta})$ is the ith element of the $\boldsymbol{B1}^+(\boldsymbol{\theta})$ vector and $B1_i^{\text{goal}}$ is the ith element of the $\boldsymbol{B1}^{+,\text{goal}}$ vector which represents the desired (objective) B_1^+ distribution.

Objective of the parameter adjustment process is to minimize the cost function with regard to the RF-input vector $\boldsymbol{\theta}$. For this purpose, the Newton minimization procedure, in particular, the steepest descent method was applied by using the 'optimization toolbox graphical interface' of MATLAB (Mathworks, Natick, MA, USA). The cost function, defined in equation (7) allows us to manipulate the magnitude of the transmit field, not taking into account its phase.

On the other hand, one very important point of this optimization procedure is the selection of the $\boldsymbol{B1}^{+,\text{goal}}$ vector. This selection is the main aspect that shifts the LCF artifact and it will be further discussed in the following sections.

4. Simulation methods

4.1. Multichannel TEM array

In order to evaluate the proposed methods, simulated data are obtained for a multichannel transmit and receive type TEM array, built in Comsol Multiphysics 5.2a (Comsol AB, Stockholm, Sweden), and post-processed in

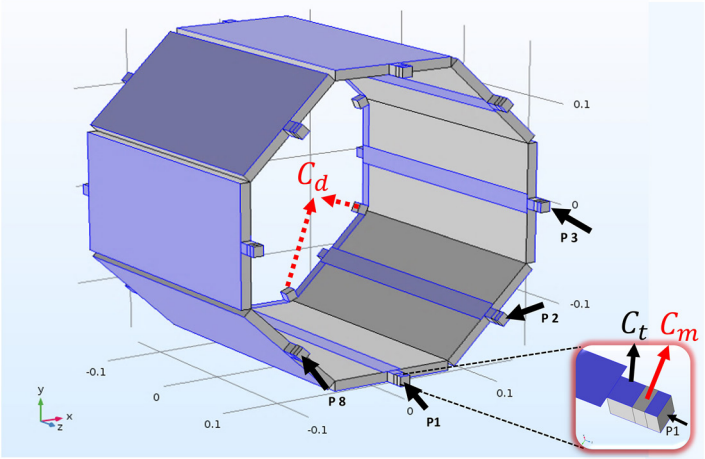

Figure 1. 8 channel TEM array, used in simulations. The purple boundaries indicate the metal layers and P1–P8 indicate the driving ports of the array. C_t and C_d are the tuning and decoupling capacitors, C_m is the series connected, lumped element defined, surface matching capacitor.

MATLAB (Mathworks, Natick, MA, USA). The octagon-shaped 8 channel TEM array has a radius of 15 cm (measured from center to the middle of each dielectric piece) and length of 30 cm, shown in figure 1.

This array is similar in structure to the one given in Adriany *et al* (2005), however, it is designed to resonate at 123.2 MHz which is for 3 T (nominal value) MRI systems. The coil comprises eight individual microstrip transmission line elements with approximately 50 Ohm characteristic impedance. The microstrip width is designed to be 2 cm, and dielectric thickness is 1 cm. The dielectric material is plexiglass and has a relative dielectric constant of $\epsilon_r = 3.6$.

For tuning, each and every microstrip transmission line element is shunted by 31.5 pF capacitors at both ends. 1 pF decoupling capacitors are connected between the line elements at the rear end of the coil, and finally, matching is accomplished with 2.5 pF series capacitors to ensure that sufficient power is transmitted to the coil. These capacitors are explicitly demonstrated in figure 1. The tuning and decoupling capacitors are constructed using the proper dielectric constants for the materials between two perfect electric conductor plates. On the other hand, the 'lumped element' boundary condition of Comsol Multiphysics is used for the series matching capacitors, in order for geometrical suitability. With these parameters, the simulated input reflection coefficients are: $S_{ii} = -40.4$ dB, for $i \in \{1, 2, 3, ..., 8\}$ and port isolations are: $S21 = -17.2$ dB, $S31 = -13.6$ dB, $S41 = -16.1$ dB, $S51 = -15.2$ dB, $S61 = -16$ dB, $S71 = -13.6$ dB and $S81 = -17.2$ dB. Due to the symmetrical geometry of the coil, there is no need for giving the complete S-matrix. With such values, sufficient matching and decoupling conditions are achieved (Vernickel *et al* 2007).

4.2. Simulation phantoms

In order to apply the algorithm, two different cylindrical simulation phantoms and a head model, as shown in figures 2 and 3 were used. The first phantom, or the so-called 'homogeneous phantom' is an object in which $\sigma = 0.5\,\mathrm{S\,m^{-1}}$ and $\epsilon_r = 80$ everywhere (for region I, shown in figure 2). For the second phantom, the phantom with anomalies, there are three regions II–IV in which $\sigma = 0.5\,\mathrm{S\,m^{-1}}, 0.85\,\mathrm{S\,m^{-1}}, 1.25\,\mathrm{S\,m^{-1}}$, and $\epsilon_r = 80, 50, 50$ respectively. Radii of both cylindrical phantoms are chosen to be 11 cm, however, data is taken from an internal 7 cm radius region. Heights of these phantoms are 30 cm and the central horizontal slice is the $z = 0$ slice. For both of the phantoms, relative permeability is taken as $\mu_r = 1$.

The reconstruction algorithm was tested for the $z = 0$ slice. Constructing the mesh of the phantom and coil, tetrahedron based, variable size mesh has been used. The maximum element size was set to be 1.75 mm for the regions inside the phantom where $-0.5\ \mathrm{cm} < z < 0.5\ \mathrm{cm}$ and inside all of the capacitors, and 1 cm for the remaining parts of the phantom and for the dielectric regions of the coil.

Analyzing the performance of the proposed algorithm on a more sophisticated and more realistic simulation phantom, a 3D head model (brain phantom) simulation was found to be necessary (Gurler and Ider 2015, 2016). Localization and mesh distribution of the 3D head model inside the TEM array is depicted in figure 3. Just like the other cylindrical phantoms, there is a central region (region II) of thickness 1 cm, having the finest mesh distribution in order to get the data with minimal noise. The maximum tetrahedral element size at the coarser regions (I and III) are chosen to be 1 cm whereas it is 1.75 mm at the finer region (II). The mesh size on the coil and at the surrounding air regions are the same as the ones in the previously described simulations.

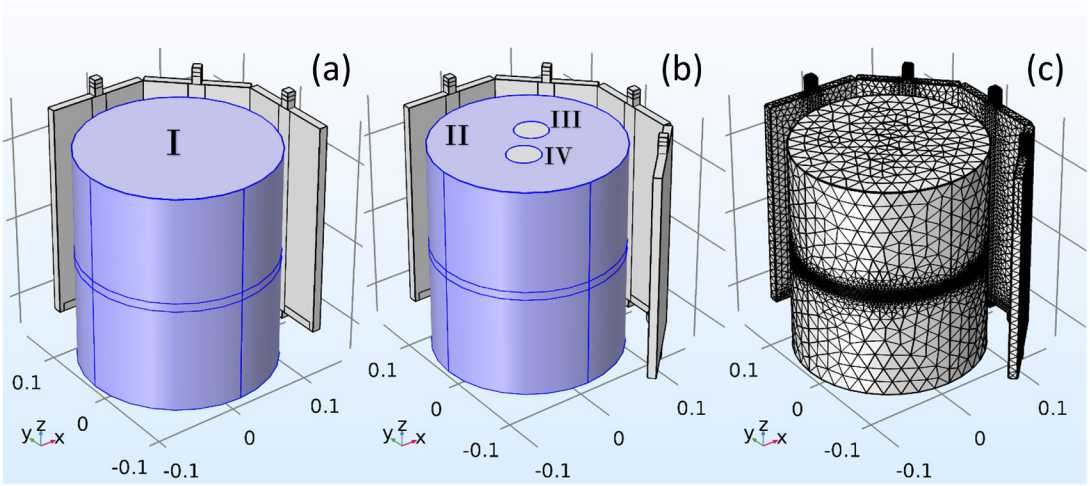

Figure 2. The simulation phantoms, shown inside the TEM array. (a) depicts the homogeneous phantom in which EPs are constant everywhere and (b) shows the phantom with two cylindrical anomalies. Regions I and II have $\sigma = 0.5\,\mathrm{S\,m^{-1}}$ and $\epsilon_r = 80$. Regions (III) and (IV) have conductivities of $\sigma = 0.85\,\mathrm{S\,m^{-1}}$ and $\sigma = 1.25\,\mathrm{S\,m^{-1}}$ respectively, and relative permittivities of $\epsilon_r = 50$ for both. (c) demonstrates the mesh distribution for both phantoms. Only three line elements of the coil are shown for better visibility of the phantom.

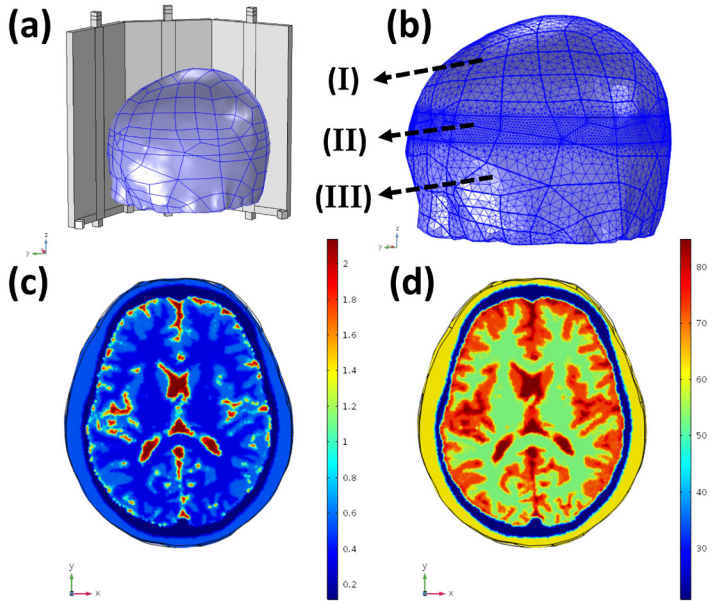

Figure 3. The localization and mesh distribution of the brain phantom in (a) and (b), respectively. The coarser mesh regions are I and III whereas the finer mesh region is shown by II. Conductivity (σ) and relative permittivity (ϵ_r) distributions at the central slice ($z = 0$, middle slice of region II) of the brain phantom are shown in (c) and (d), respectively.

The head model shown in figure 3 has internal conductivity and permittivity distributions, being compatible with the conductivity and permittivity of the internal regions of a human head. Being segmented into five tissues, namely cerebrospinal fluid (CSF), white matter (WM), gray matter (GM), skull and scalp, the approximate conductivity distributions of these tissues are respectively given as 2.14, 0.34, 0.59, 0.12 and 0.54 $\mathrm{S\,m^{-1}}$ and their approximate relative permittivity values are given as 84, 52, 73, 21 and 62 (Gabriel *et al* 1996, Michel *et al* 2016, Gurler and Ider 2015). The conductivity and relative permittivity distributions, shown at the center slice ($z = 0$) of the brain phantom are also demonstrated in figure 3.

5. Results

5.1. EP reconstructions obtained with the normal drive

For the homogeneous cylindrical phantom, B_1^+ magnitude, F_x magnitude and EP reconstructions using the cr-MREPT method are shown in figure 4 for the case where the coil is driven by 1 V of peak amplitude and 45 degree

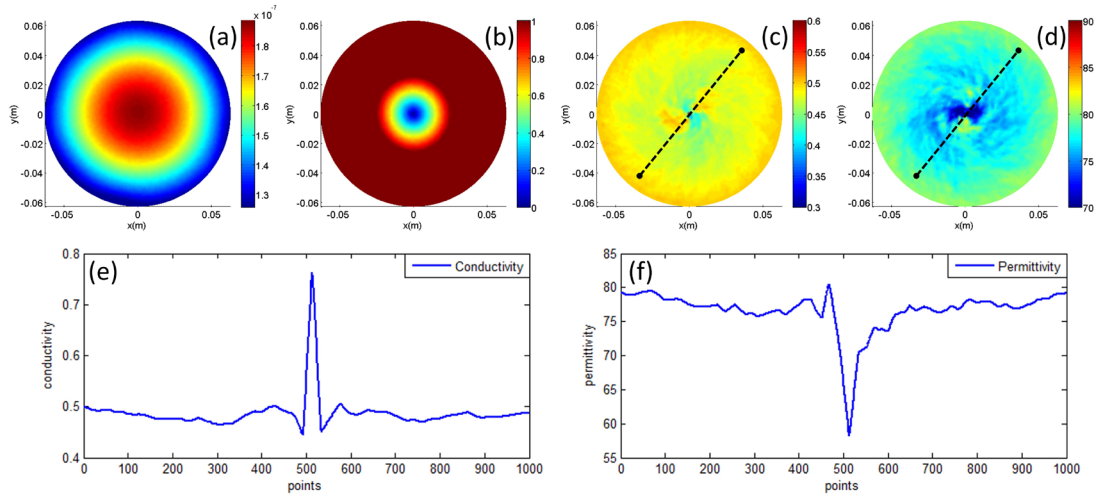

Figure 4. The B_1^+ magnitude, F_x magnitude, conductivity reconstruction (S m^{-1}) and relative permittivity reconstruction given in (a)–(d), respectively. (e) and (f) Shows profile plots of conductivity and relative permittivity along the dashed lines on (c) and (d).

phase increment between the adjacent ports of the TEM array. This driving case will be referred to as the 'normal drive' in the subsequent sections.

As it is clear from figure 4, the place at which the convective field magnitude significantly decreases is the center region and at that region, the abrupt positive and negative jumps at the EP reconstructions refer to the classically known 'LCF-artifact'. Furthermore, slow variations in the EPs around the LCF artifacts, extending over larger regions, are observed in figures 4(c) and (d). This phenomenon is called the 'global bias' on the EP reconstructions, being obtained by the cr-MREPT method (Liu *et al* 2017).

5.2. The modified B_1^+ distribution

In order to shift the location of the LCF regions, a proper $B_1^{+,\mathrm{goal}}$ ($\boldsymbol{B1}^{+,\mathbf{goal}}$ is the discretized single-column version of the continuous $B_1^{+,\mathrm{goal}}$) needs to be specified. Deciding on that, results of using different $B_1^{+,\mathrm{goal}}$ distributions as well as the results of different shimming methods (described below) have been considered and compared.

Among the cases covered in this study, the $B_1^{+,\mathrm{goal}}$ magnitude in the ROI shown in figure 5, which has high B_1^+ magnitude on one half and a low B_1^+ magnitude on the other half is chosen as the best distribution. The value of the B_1^+ magnitude in the higher half of the goal distribution (high field region), is chosen to be equal to the maximum B_1^+ magnitude value of the homogeneous phantom when the normal drive is used. For the lower part, (low field region) B_1^+ magnitude is assigned as one-tenth of the value in the higher part. By choosing such a $B_1^{+,\mathrm{goal}}$ distribution, it is obviously not expected to obtain a modified B_1^+ distribution with a discontinuous transition in the middle due to the fact that electromagnetic wavelength in the phantom with $\epsilon_r = 80$ is approximately 27 cm (at 123.2 MHz). The purpose is to force the modified B_1^+ distribution to have a relatively sharp variation in the middle region.

As different $\boldsymbol{B1}^{+,\mathbf{goal}}$ distributions and different shimming methods are considered, their practical feasibility turns out to be crucial.

One physical limitation in this regard is that the ratio between the high field and low field regions need to be as low as possible in order to avoid significant signal to noise ratio (SNR) differences between them for the viability of implementation in an MRI scanner. Throughout our trials, as shown in figure 6, it has been observed that a ratio of two (2×) is not sufficient to significantly shift the LCF regions. On the other hand, a ratio of five (5×) yields a nicely shifted LCF region for the homogeneous phantom, though it does not substantially shift these regions for more complicated phantoms, such as the brain model. Consequently, a ratio of ten (10×) has been found as the most stable and efficient one in terms of sufficiently shifting the LCF regions away from the center and allowing accurate EP reconstructions at the center of each and every phantom. The resultant $|B_1^+|$ and $|F_x|$ distributions for the aforementioned cases are juxtaposed in figure 6.

Another physical obstruction is that the transmitter array of an MRI scanner may not be able to send the desired voltages to the input ports of the RF coil (due to imperfections on input matching) hence the peak amplitude ratios among different inputs should not be arbitrarily large. In order to avoid this issue, a phase-only parameter adjustment method for attaining the $B_1^{+,\mathrm{goal}}$ with a ratio of ten between the high and low field regions has been used. In this case, the same optimization algorithm in section 3.1 was conducted where the amplitudes

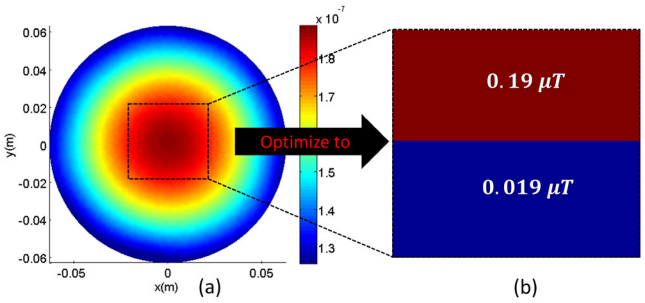

Figure 5. (a) A general B_1^+ magnitude image of a circular phantom of constant conductivity and permittivity. The central region in (a) (the indicated square) is the region where $B_1^{+,\text{goal}}$ is specified. (b) The optimization goal for the B_1^+ magnitude.

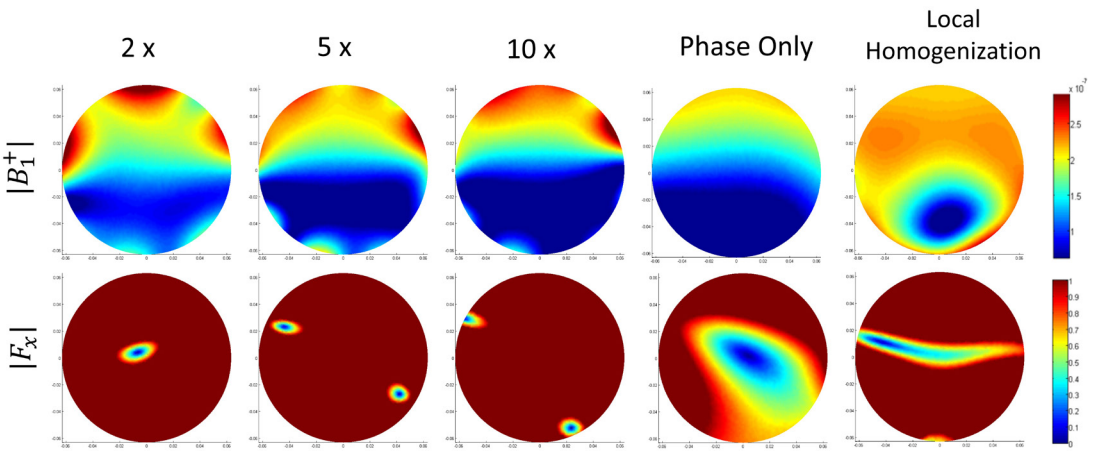

Figure 6. The B_1^+ magnitude (Tesla) and F_x magnitude distributions for the $2\times, 5\times, 10\times$ cases as well as for the phase-only optimization and slice homogenization (Ibrahim 2006) methods.

of the RF inputs were forced to be the same. However, this procedure also turned out to be insufficient for significantly shifting the LCF regions, as shown in figure 6.

Finally, two commonly used B_1^+ shimming strategies, described as the 'localized' and 'whole-slice homogenized' RF field excitations (Ibrahim 2006) are considered to be nice candidates for shifting the LCF artifact since one can attain a varying B_1^+ magnitude at the center, when these methods are properly used. According to our objective, 'localized RF excitation' turns out to be inconvenient since it tries to maximize the B_1^+ magnitude at a particular region, yielding an extremely low B_1^+ magnitude distribution at the non-localized regions. In this case, the B_1^+ magnitude ratio between the localized and non-localized regions can be as great as 100, which is completely problematic for our case, as described. On the other hand, the 'whole body excitation' in Ibrahim (2006) can be adapted to minimize the homogeneity coefficient defined as the standard deviation of B_1^+ over the mean of B_1^+ in a particular region, rather than the whole slice. The underlying idea for such an attempt is the presumption that the LCF region may shift towards the homogenized region, in parallel with the ideas developed in the last paragraph of section 2.2. For the cases in this study, the homogeneity coefficient at the red-colored region in figure 5(b) is homogenized and the resulting B_1^+ magnitude and F_x magnitude are demonstrated in figure 6. Apparently, this method is also not effective in significantly shifting the LCF artifact.

To this end, the magnitude and phase values of the port RF inputs for $10\times$ case are depicted in table 1. This driving configuration is explicitly referred to as the 'modified drive' configuration.

5.3. The combined EP reconstructions

Having acquired the B_1^+ distributions from the normal and the modified drive configurations, our objective is to make simultaneous use of the two datasets to obtain the so-called 'combined reconstructions', as explained in section 2.1.

The combined EP reconstructions, as well as the EP reconstructions from the modified drive only are shown in figure 7 for the homogeneous phantom. As it can be seen from figures 7(a) and (c), the modified drive spatially shifts the LCF artifact (as shown by the arrows in the figure) and the global bias on the EP reconstructions just as it shifts the LCF region as shown in figure 6, $10\times$ case. When the combined reconstructions in figures 7(b) and (d) are considered, it is observed that the LCF artifacts are eliminated throughout the whole slice.

Table 1. RF input signal magnitude and phase values for the modified drive. These values are the exact ones acquired with the modification algorithm in section 3.1. However, mean value of the phases is irrelevant and can be subtracted while using them.

Ports	1	2	3	4	5	6	7	8
Magnitude (V)	9.5	11.8	9.4	8.7	7.6	10.7	12.1	7.8
Phase (Rad)	−2.6	−2.7	−2.9	−2.5	−2.5	−2.5	−3.0	−2.8

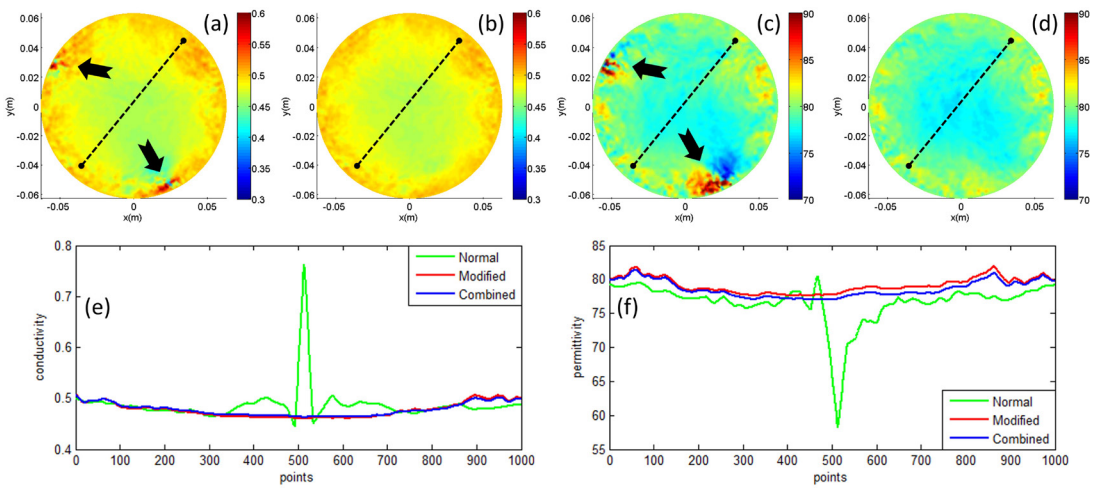

Figure 7. (a) and (b) Modified and combined conductivity reconstructions (in S m^{-1}), (c) and (d): modified and combined relative permittivity reconstructions. (e) and (f) Profile plot of conductivity and relative permittivity reconstructions along the dashed lines on (a)–(d) for normal drive, modified drive and combined cases.

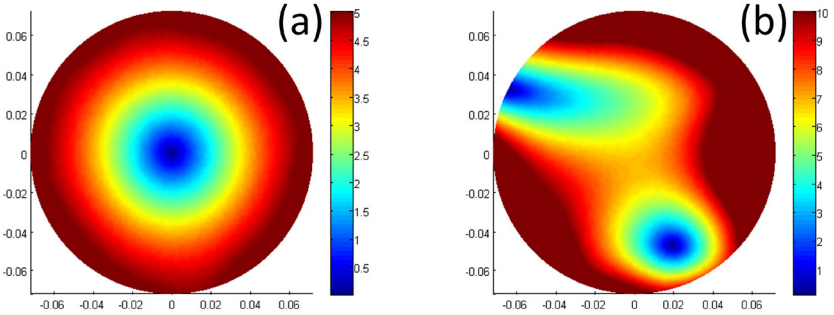

Figure 8. (a) E_z magnitude for normal drive, (b) E_z magnitude for modified drive. Both of the images belong to the homogeneous phantom.

As stated in the theory section, figure 8 shows the magnitude of the z component of the electric field for the normal and modified drive cases. Compared with the F_x distributions for normal and modified drive cases in figures 4 and 6, this figure clearly demonstrates that there is a direct correlation between F_x and E_z as stated in the theory section.

After using the procedure of B_1^+ optimization for the homogeneous phantom, the exact same RF amplitude and phase values for the normal and modified drive cases are applied to the phantom with anomalies as well. The B_1^+ magnitude, F_x and EP reconstructions with cr-MREPT method for normal and modified drive, as well as the combined EP reconstructions are demonstrated in figure 9. As we scrutinize the B_1^+ magnitude of the modified drive in figure 9(e), the existence of a high and low field region separation similar to the homogeneous phantom case becomes evident, though this separation is not as optimal as in the homogeneous case. On the other hand, figures 9(b) and (f) clearly demonstrate that also in the phantom with anomalies, the LCF regions are significantly shifted and do not overlap. In parallel with this observation, the LCF artifacts in the EP reconstructions are also shifted. When the combined reconstructions in figures 9(i) and (j) are examined, it is clear that both the LCF artifacts and global biases are significantly eliminated.

Although the RF amplitude and phase values in table 1, which are designed for the homogeneous phantom, are used for the phantom with anomalies, it became possible to sufficiently alleviate the LCF artifact and the global biases. Using the same modified input RF signals for different phantoms significantly facilitates the experimental process by getting rid of the need for another modification procedure for every object to be imaged inside the TEM array.

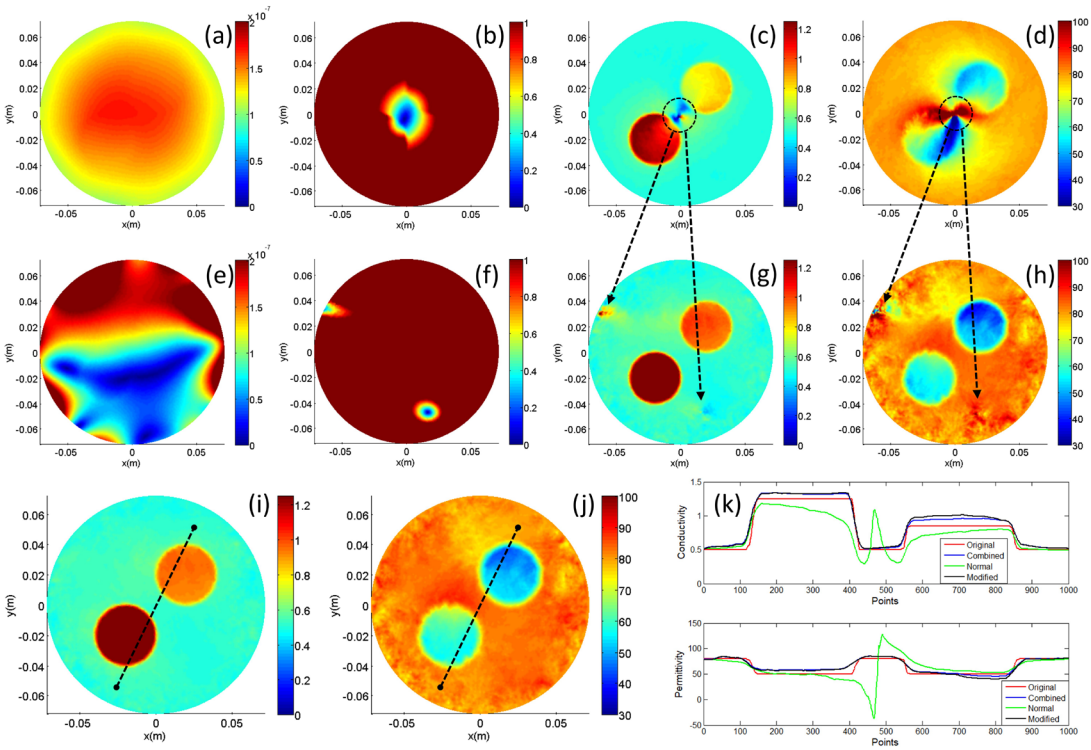

Figure 9. Results of the phantom with anomalies: ((a) and (e)) B_1^+ magnitude, ((b) and (f)) F_x magnitude, ((c) and (g)) conductivity reconstructions (S m^{-1}), ((d) and (h)) relative permittivity reconstructions for the normal and modified drive respectively, (i) combined conductivity reconstruction, (j) combined relative permittivity reconstruction and (k): profile plots of original conductivity and relative permittivities (red) as well as profile plots of the reconstruction results for the normal drive (green), modified drive (black) and combined reconstruction (blue) cases. The profiles are taken along the dashed lines in (i) and (j).

5.4. Head model results

The head model is simulated using the same RF magnitudes and phases as used in the previous phantom simulations. The B_1^+ magnitudes, F_x magnitudes and EP reconstructions the for normal and modified drive are demonstrated in figure 10.

Considering figure 10, it can be seen that the low convective fields occur at the center of the brain phantom for the normal drive case, being similar to the cylindrical phantoms. As figure 10(e) is examined, it seems that the input RF sinusoids in table 1 provides the separation of high and low field regions even for the head model. Examining figures 10(b) and (f), the shift in LCF artifact when the modified drive is applied, can become clear. The combined solution shown in figure 10(i) clearly demonstrates an improved conductivity reconstruction, being much more accurate than the solutions from individual drives. Although the permittivity reconstructions of the normal drive have overestimated results at the CSF regions, just as reported in Hafalir *et al* (2014), the modified drive is able to shift the LCF artifact on the permittivity reconstructions as well, yielding artifact-free combined permittivity reconstructions. From the same figure, the profile plots along the dashed lines on (i) and (j) better show this situation.

5.5. Boundary performance analysis

An important issue in EPT studies is the performance of the EP reconstruction algorithms at the tissue boundaries. It has been shown for the Helmholtz based algorithms that these performances are lowered as the difference between the EP values of the adjacent tissues of the boundaries gets larger (Duan *et al* 2017). As stated earlier in the introduction, methods such as cr-MREPT which take into consideration that EP gradients are not negligible, give much more accurate EP reconstructions at the boundaries. While the methods developed in this study eliminate the LCF artifact of cr-MREPT, it is of interest to consider if the boundary reconstruction performance is enhanced or sacrificed.

To analyze this performance, we started with detecting the internal EP boundaries within 'regions of analyses' on the head model and on the phantom with anomalies. The EP edges are first detected on a Cartesian grid and the nodes of our triangular mesh which lie on both sides of and on these edges are determined, similar to in Duan *et al* (2017). Absolute values of the difference between the original and reconstructed EP distributions on these nodes are calculated and shown in figure 11 for the 'normal drive' (original cr-MREPT), 'combined reconstruction' and 'standard (conventional) MREPT' (Voigt *et al* 2011) cases. For the brain phantom, most of the

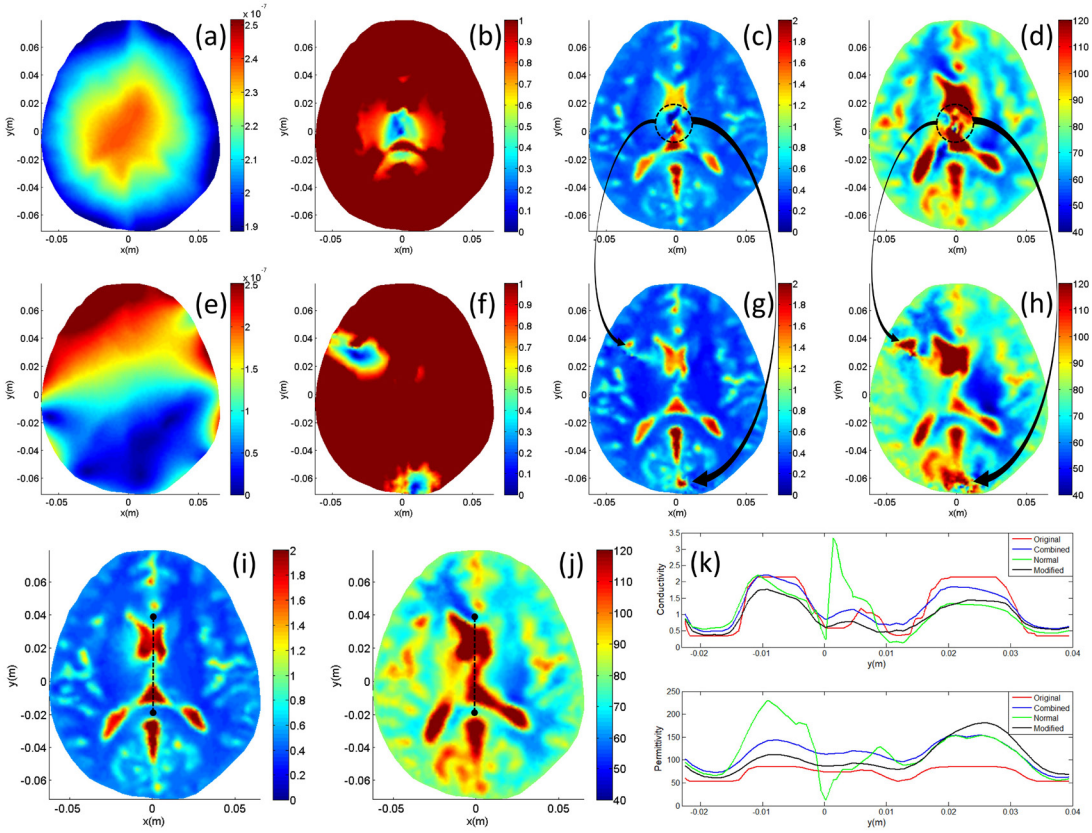

Figure 10. Head model results: ((a) and (e)) B_1^+ magnitude, ((b) and (f)) F_x magnitude, ((c) and (g)) conductivity reconstructions (S m^{-1}), ((d) and (h)) relative permittivity reconstructions for the normal and modified drive respectively, (i) combined conductivity reconstruction, (j) combined relative permittivity reconstruction and (k) profile plots of original conductivity and relative permittivities (red) as well as profile plots of the reconstruction results for the normal drive (green), modified drive (black) and combined reconstruction (blue) cases. The profiles are taken along the dashed lines in (i) and (j).

analyzed boundaries include the CSF- gray matter adjacency. As it can be seen from the figure, both the normal drive and combined reconstructions give similar errors in non-LCF regions which are much less than the errors of the Standard MREPT. On the other hand, some of the EPs at the tissue boundaries close to the center of the phantom and head model (the LCF regions) are reconstructed with better accuracy than the original cr-MREPT with the proposed method (combined case), as indicated by the arrows on figure 11.

In order for quantitatively describing these results, as in Liu *et al* (2015) and Duan *et al* (2017), the mean relative reconstruction error metrics along the boundaries are defined as in the following:

$$rRE_\sigma = \sqrt{\frac{1}{N}\sum_{i=1}^{N}\frac{(\sigma_i^* - \sigma_i)^2}{\sigma_i^2}} \; rRE_{\epsilon_r} = \sqrt{\frac{1}{N}\sum_{i=1}^{N}\frac{(\epsilon_{ri}^* - \epsilon_{ri})^2}{\epsilon_{ri}^2}} \tag{8}$$

where σ_i and ϵ_{ri} are the original conductivity and relative permittivity values and σ_i^* and ϵ_{ri}^* are the reconstructed conductivity and relative permittivity values of the ith data point along the boundaries. Furthermore, N is the total number of data points along the boundary. The numerical relative reconstruction errors found with equation (8) are depicted in table 2 below.

As it can be inferred from the table, the combined reconstruction not only does not compromise the boundary performance of original cr-MREPT, but also enhances it for the cases where the low convective field regions coincide with the tissue boundaries, especially for the phantom with anomalies.

5.6. Noise analysis

Behavior of the proposed method against noise contamination is an important step in terms of the feasibility of the algorithm since it uses the 'modified drive' in which there is nearly 10 times B_1^+ magnitude difference between the two sides (i.e. high field-low field regions) of the phantom.

In order to analyze the behavior of the algorithm against noise, white-Gaussian noise is added to the real and imaginary parts of the simulated complex B_1^+ distribution. Simulated noise is adjusted by setting the standard deviation of the normal distribution to $(1/K)$ times the mean value of the B_1^+ magnitude. It should be noted that reciprocal of K is representative of the strength of noise (Liu *et al* 2017). Brain phantom is chosen

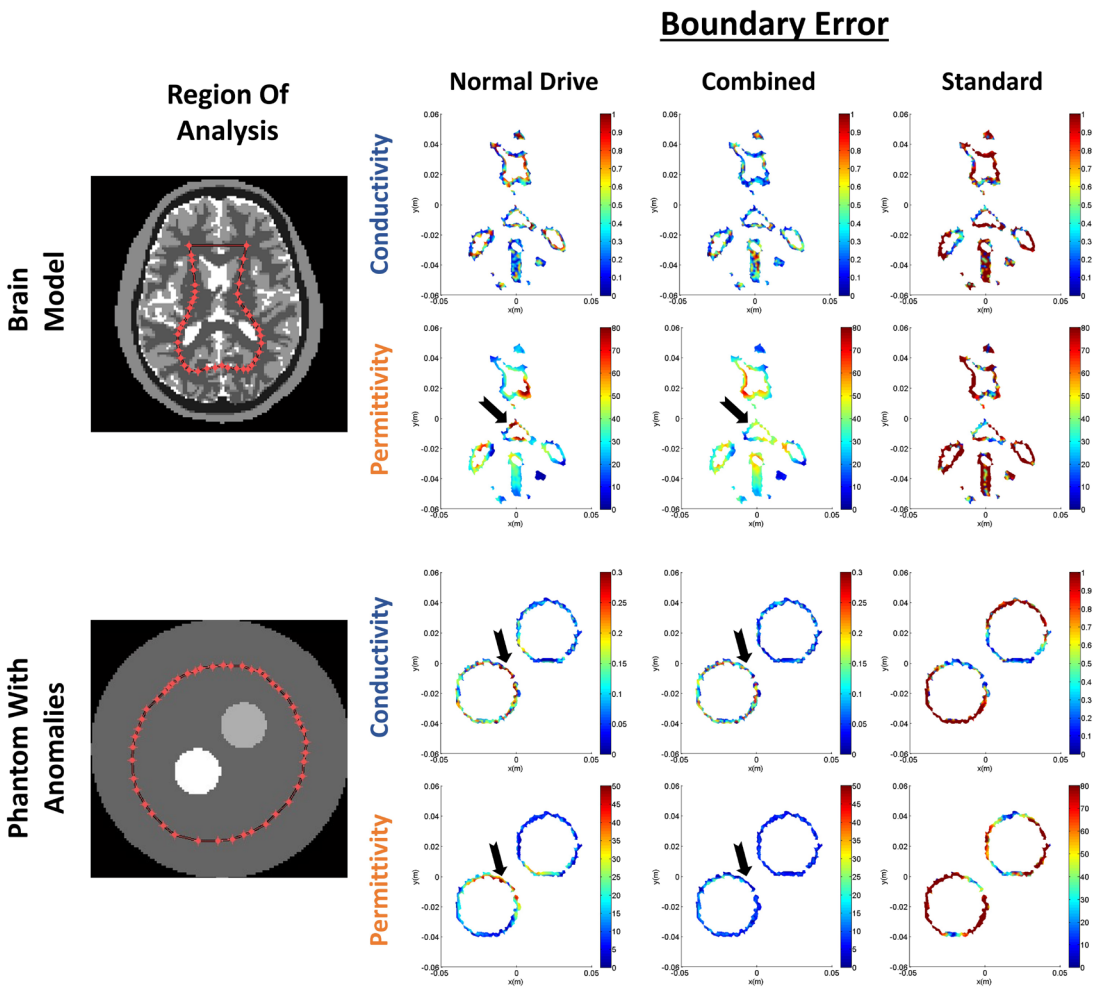

Figure 11. Boundary analysis results: the red dotted polygons below the heading 'region of analysis' (ROA) demonstrates the regions in which the interior tissue boundaries are detected. Absolute value of the difference between original EP distributions and reconstructed ones along the boundaries within the ROA are shown for the 'normal drive' (original cr-MREPT), 'combined reconstructions' and 'standard MREPT' cases.

Table 2. Mean relative reconstruction errors along the boundaries for the brain phantom and the phantom with anomalies. These are calculated with equation (8).

		Normal	Combined	Standard
Brain	Conductivity (S m^{-1})	0.424	0.426	1.6704
	Relative permittivity (ϵ_r)	0.530	0.526	2.180
Phantom	Conductivity (S m^{-1})	0.183	0.147	1.881
	Relative permittivity (ϵ_r)	0.327	0.156	1.769

for analyzing the noise performance of the proposed method. After the noise is added, the noisy B_1^+ distributions are filtered with a 2D low pass filter with a 3×3 Gaussian kernel and a standard deviation of 2 pixels. The combined EP reconstruction results with K values 200, 300, 400 and 1×10^6 (no noise) are depicted in figure 12.

With the reconstructions, which were made using the noisy data, it seems reasonable to state that the noise behavior of the cr-MREPT algorithm is acceptable except for $K = 200$ case for the conductivity reconstructions. On the other hand, the permittivity reconstructions tend to be much more vulnerable to noise contamination, as stated in Hafalir *et al* (2014) and Li *et al* (2017) and need even better K values than 400. Therefore, the MRI images should be obtained with the highest SNR possible to get accurate measurements.

6. Conclusion and discussion

Throughout this paper, an improved cr-MREPT method has been proposed. The simulation results show that the improvement procedure is a nice candidate for alleviating the global biases and LCF artifacts.

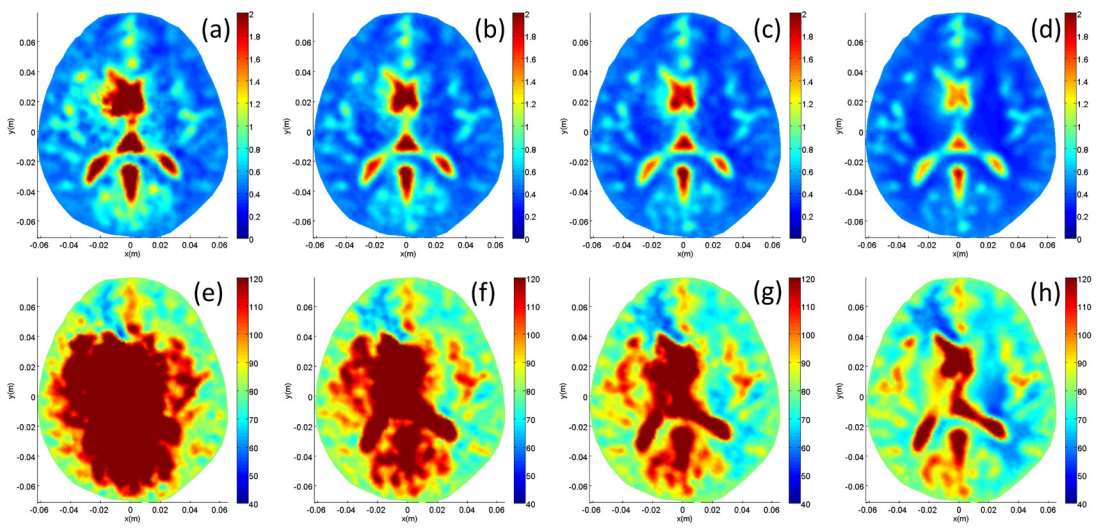

Figure 12. Noise analysis of the brain phantom: (a)–(d) combined conductivity and (e)–(h) combined relative permittivity reconstructions for K values of 200, 300, 400 and 1×10^6 (no noise) respectively.

An important point of emphasis is that the method can be applied in clinical studies without requiring an optimization process for every patient. The issue of the necessity of a patient-specific B_1^+ modification was thoroughly examined in Van den Berg *et al* (2007), in terms of reducing the specific absorption rate (SAR) at specific regions. In that study, it was concluded that although a superior B_1^+ shimming is possible with patient-specific B_1^+ optimization, adjusting the input RF sinusoids for an elliptical phantom—similar to human body size—and using them for every patient becomes considerably effective. The situation is similar in our application: Although it is obvious that optimizing the input RF sinusoids for every patient will give better modified B_1^+ distributions, the modified RF inputs designed for a cylindrical phantom also work for the human head.

In order for implementing the proposed method, retrieval of the transmit B_1^+ magnitude and absolute transmit phase ($\phi(B_1^+)$) is essential. Magnitude of the transmit fields ($|B_1^+|$) for the normal drive, modified drive and also for the individual transmit channels (necessary for the optimization procedure) can be found by one of the established B_1^+ mapping procedures as in Cunningham *et al* (2006).

On the other hand, there is no straightforward method for measuring the phase of B_1^+ because in any transmit-receive configuration, the phase of the image is the sum of the transmit and the receive phases (Van de Moortele *et al* 2005) (assuming B_0 inhomogeneity and eddy current contributions, etc are eliminated by proper sequence design). Transmit phase of the normal drive can be estimated using TPA for 3 T MRI systems (Katscher *et al* 2009). However, finding the transmit phase for the modified drive and the transmit phases of the individual channels (again necessary for the optimization procedure), we need other methods.

Several methods for estimating the phase of B_1^+ have been proposed (Van de Moortele *et al* 2005, Katscher *et al* 2012, Liu *et al* 2015). In Katscher *et al* (2012), a method is developed for estimating the B_1^+ phase distributions of each transmit channel of a multichannel array such that their method also applies for non-quadrature RF excitation. In Liu *et al* (2015), multiple transmit-receive configuration data are used to estimate the derivatives of a reference coil's transmit and receive phases from which derivatives of the phases of other channels can be calculated. Local Maxwell tomography (LMT) (Sodickson *et al* 2012a) and generalized local Maxwell tomography (Sodickson *et al* 2012b) also attempt to estimate the derivatives of the phases of RF magnetic fields of a multichannel system based on many data sets from many transmit-receive combinations. While LMT makes use of local homogeneity assumption, generalized LMT does not. These methods can be used to implement our proposed algorithm, however, they involve several assumptions and practical issues and therefore their experimental validation for use in our algorithm is very important.

Acknowledgments

This work was supported by The Scientific and Technological Research Council of Turkey (Tubitak) under Grant 114E522.

References

Abraham R and Ibrahim T S 2007 Proposed radiofrequency phased-array excitation scheme for homogenous and localized 7-tesla whole-body imaging based on full-wave numerical simulations *Magn. Reson. Med.* **57** 235–42.

Adriany G *et al* 2005 Transmit and receive transmission line arrays for 7 T parallel Imaging *Magn. Reson. Med.* **53** 434–45
Balidemaj E *et al* 2015 CSI-EPT: a contrast source inversion approach for improved MRI-based electric properties tomography *IEEE Trans. Med. Imaging* **44** 1788–96
Birgul O and Ider Y Z 1995 Use of magnetic field generated by the internal distribution of injected currents for electrical impedance tomography *Proc. of 9th Int. Conf. on Electrical Bio-Impedance in Conjunction with European Concerted Action on Impedance Tomography (Heidelberg)* pp 418–9
Borsic A, Perreard I, Mahara A and Halter R J 2016 An inverse problems approach to MR-EPT image reconstruction *IEEE Trans. Med. Imaging* **35** 244–56
Cunningham C H, Pauly J M and Nayak K S 2006 Saturated double-angle method for rapid B1 mapping *Magn. Reson. Med.* **55** 1326–33
Duan S *et al* 2017 Quantitative analysis of the reconstruction errors of the currently popular algorithm of magnetic resonance electrical property tomography at the interfaces of adjacent tissues *NMR Biomed.* **29** 744–50
Gabriel S *et al* 1996 The dielectric properties of biological tissues: III. Parametric models for the dielectric spectrum of tissues *Phys. Med. Biol.* **41** 2271–93
Griffiths H 2001 Magnetic induction tomography *Meas. Sci. Technol.* **12** 1126–31
Gurler N 2016 Multichannel, phase based magnetic resonance electrical properties tomography *PhD Thesis* Bilkent University
Gurler N and Ider Y Z 2015 Numerical methods and software tools for simulation, design, and resonant mode analysis of radio frequency birdcage coils used in MRI *Concepts Magn. Reson.* **45** 13–32
Gurler N and Ider Y Z 2016 Gradient- based electrical conductivity imaging using MR phase *Magn. Reson. Med.* **77** 137–50
Gurler N, Oran O F and Ider Y Z 2015 Combination of multichannel receive data for local Cr-MREPT *Proc. of the 23th Annual meeting of ISMRM (Toronto, Ontario, Canada)*
Hafalir F S, Oran O F, Gurler N and Ider Y Z 2014 Convection-reaction equation based magnetic resonance electrical properties tomography (cr-MREPT) *IEEE Trans. Med. Imaging* **33** 456–66
He B *et al* 2011 Electrophysiological imaging of brain activity and connectivity-challenges and opportunities *IEEE Trans. Med. Imaging* **58** 1918–31
Holder D S 1993 Detection of cerebral ischaemia in the anaesthetised rat by impedance measurement with scalp electrodes: implications for non-invasive imaging of stroke by electrical impedance tomography *Clin. Phys. Physiol. Meas.* **13** 63–75
Ibrahim T S 2006 Ultrahigh-field MRI whole-slice and localized RF field excitations using the same RF transmit array *IEEE Trans. Med. Imaging* **25** 1341–7
Ider Y Z and Birgul O 1998 Use of the magnetic field generated by the internal distribution of injected currents for electrical impedance tomography (MR-EIT) *Turk. J. Electr. Eng. Comput. Sci.* **6** 215–25
Joines W T, Zhang Y, Chenxing L and Jirtle L 1994 The measured electrical properties of normal and malignant human tissues from 50 to 900 MHz *Med. Phys.* **21** 547–50
Katscher U, Findeklee C and Voigt T 2012 B_1-based specific energy absorption rate determination for nonquadrature radiofrequency excitation *Magn. Reson. Med.* **68** 1911–8
Katscher U *et al* 2009 Determination of electric conductivity and local SAR via B_1 mapping *IEEE Trans. Med. Imaging* **28** 1365–74
Li C, Yu W and Huang S Y 2017 An MR-based viscosity-type regularization method for electrical property tomography *Tomography* **25** 50–9
Liu J, Wang Y, Katscher U and He B 2017 Electrical properties tomography based on B_1 maps in MRI: principles, applications and challenges *IEEE Trans. Biomed. Eng.* **64** 2515–30
Liu J *et al* 2015 Gradient-based electrical properties tomography (gEPT): a robust method for mapping electrical properties of biological tissues *in vivo* using magnetic resonance imaging *Magn. Reson. Med.* **74** 634–46
Liu Z *et al* 2006 Noninvasive reconstruction of three-dimensional ventricular activation sequence from the inverse solution of distributed equivalent current density *IEEE Trans. Med. Imaging* **25** 1307–18
Michel E, Hernandez D and Lee S Y 2016 Electrical conductivity and permittivity maps of brain tissues derived from water content based on T1-weighted acquisition *Magn. Reson. Med.* **77** 1094–103
Nachman A, Wang D, Ma W and Joy M 2007 A local formula for inhomogeneous complex conductivity as a function of the RF magnetic field *Proc. of the 15th Annual Meeting of ISMRM (Berlin, Germany)*
Romsauerova A, McEwan A, Horesh L, Yerworth R, Bayford R H and Holder D S 2006 Multi-frequency electrical impedance tomography (EIT) of the adult human head: initial findings in brain tumours, arteriovenous malformations and chronic stroke, development of an analysis method and calibration *Physiol. Meas.* **27** 147–61
Ropella K M and Noll D C 2017 A regularized, model-based approach to phase-based conductivity mapping using MRI *Magn. Reson. Med.* **78** 2011–21
Serralles J E C *et al* 2017 Global Maxwell tomography: a novel technique for electrical properties mapping without symmetry assumptions or edge artifacts *Proc. of the 24th Annual Meeting of ISMRM (Singapore)*
Sodickson D K *et al* 2012a Local Maxwell tomography using transmit-receive coil arrays for contact-free mapping of tissue electrical properties, determination of absolute RF phase *Proc. of the 20th Annual meeting of ISMRM (Melbourne, Australia)*
Sodickson D K *et al* 2012b Generalized local Maxwell tomography for mapping of electrical property gradients, tensors *Proc. of the 20th Annual Meeting of ISMRM (Melbourne, Australia)*
Surowiec A J, Stuchly S S, Barr J R and Swarup A 1988 Dielectric properties of breast carcinoma and the surrounding tissues *IEEE Trans. Biomed. Eng.* **35** 257–63
Van de Moortele P F *et al* 2005 B_1 destructive interferences and spatial phase patterns at 7 T with a head transceiver array coil *Magn. Reson. Med.* **54** 1503–18
Van den Berg C A T *et al* 2007 Simultaneous B_1^+ homogenization and *specific* absorption rate hotspot suppression using a magnetic resonance phased array transmit coil *Magn. Reson. Med.* **57** 577–86
Van Lier A L H M W *et al* 2012 B_1^+ phase mapping at 7 T and its application for *in vivo* electrical conductivity mapping *Magn. Reson. Med.* **67** 552–61
Vernickel P *et al* 2007 Eight-channel transmit/receive body MRI coil at 3 T *Magn. Reson. Med.* **58** 381–9
Voigt T, Katscher U and Doessel O 2011 Quantitative conductivity and permittivity imaging of the human brain using electric properties tomography *Magn. Reson. Med.* 456–66
Yildiz G, Ariturk G and Ider Y Z 2017 Use of padding to eliminate low convective field artifact in conductivity maps obtained by cr-MREPT *Proc. of the 25th Annual Meeting of ISMRM (Honolulu, HI, USA)*